RSC Advances

PAPER

View Article Online
View Journal | View Issue

Cite this: *RSC Adv.*, 2026, **16**, 13114

Solvent-mediated organocatalytic browning of biogenic indoles enables the formation of zwitterionic nanoparticles

Teh-Min Hu, *[a] Hsin-Hui Lin,[ab] Chun-Yi Huang,[a] Mei-Hsiang Lin[b] and Shih-Jiuan Chiu[b]

Received 20th December 2025
Accepted 25th February 2026

DOI: 10.1039/d5ra09863g

rsc.li/rsc-advances

Solvent-mediated browning has recently emerged as a distinctive mode of chemical transformation in solution-phase chemistry. In this study, we extend this concept to biogenic indoles and show that an organocatalytic browning process can be achieved in a mixed DMSO/acetone system under mild, catalyst-free conditions. Tryptamine, a decarboxylated metabolite of L-tryptophan, underwent spontaneous browning despite lacking the zwitterionic framework characteristic of amino acids. Notably, the presence of indole-3-acetic acid (I3AA) markedly intensified the reaction and accelerated mesityl oxide formation, indicating a cooperative catalytic effect on acetone self-condensation. Upon transfer of the browned reaction mixtures into water, the hydrophobic products became supersaturated and spontaneously assembled into uniform nanoparticles *via* liquid–liquid nanoprecipitation. The resulting browned indole-derived nanoparticles exhibited spherical morphology, pH-responsive surface charge reversal near pH 9, and stable electrostatic association with the model polynucleotide G3139. Overall, this work illustrates how intermolecular interactions and reaction chemistry in organic solvents can be coupled with solvent exchange to drive the bottom-up formation of zwitterionic soft-matter nanostructures, providing a simple and versatile route to biogenic colloidal systems.

1. Introduction

Chemical transformations in solution can give rise not only to new reaction pathways but also to emergent soft-matter structures driven by intermolecular interactions. Biogenic indoles represent a chemically versatile class of molecules with rich reactivity in solution, enabled by their electron-rich aromatic rings, hydrogen-bonding capability, and biological relevance.[1–3]

Indole-based compounds are ubiquitous across microorganisms, plants, and animals.[4–11] Their biosynthesis primarily originates from the shikimate pathway, with chorismate serving as the precursor of L-tryptophan, the universal metabolic progenitor of diverse indole metabolites.[5] In plants and microbes, indole derivatives such as indole-3-acetic acid (I3AA) and indole-3-acetaldehyde function as growth regulators and signaling mediators,[6,7] whereas in animals, tryptamine, serotonin, and melatonin serve critical neurotransmission and neuromodulatory roles.[8–10]

Beyond biological functions, the indole scaffold is widely recognized as a privileged motif in medicinal chemistry,[3,4,12–17] forming the pharmacophoric core of nonsteroidal anti-inflammatory drugs (*e.g.*, indomethacin and sulindac), anticancer alkaloids (vincristine and vinblastine), antimigraine therapy (sumatriptan), and antihypertensive or anxiolytic agents (reserpine, buspirone).[12–17] This broad utility reflects the notable duality of the indole π system: it can participate in hydrogen bonding while preferentially undergoing electrophilic substitution, resulting in high chemical and supramolecular versatility.[3]

Importantly, indole derivatives are intrinsically predisposed to self-assembly through π–π stacking, hydrogen bonding, and hydrophobic interactions.[18–21] Such behavior is well documented biologically in tryptophan-rich domains of proteins,[18,19] in melanin biosynthesis,[20] and in amyloid fibrillation.[21] Technologically, indole-containing molecules have been used to generate soft functional materials,[22–27] including tryptophan-based hydrogels[22–24] and serotonin-derived nanoparticles and films.[25–27] Despite these advances, molecular-to-colloidal transformation of biogenic indoles remains underexplored, especially through liquid-phase chemical routes.

Maillard reactions—well-known from daily-life food chemistry—have been recognized for over a century.[28,29] Classically, they involve the non-enzymatic browning of amino acids with reducing sugars under high-temperature conditions in aqueous media yielding complex, heterogeneous reaction mixtures that remain only partially characterized even today.[28–31] In contrast to this sugar-dependent, thermally driven pathway, we

[a]*Department of Pharmacy, College of Pharmaceutical Sciences, National Yang Ming Chiao Tung University, Yangming Campus, Taipei 112304, Taiwan. E-mail: tehmin@nycu.edu.tw*

[b]*School of Pharmacy, Taipei Medical University, Taipei 110301, Taiwan*

previously identified a distinct browning chemistry in which amino acids[32–35] or proteins[32,36] undergo spontaneous coloration in organic solvent mixtures of dimethyl sulfoxide (DMSO) and acetone at room temperature, without added sugars, catalysts, or external energy input.[32–36] In this simple three-component system (amino acid, DMSO, and acetone), amino acids act as organocatalysts that activate and promote the self-aldol condensation of acetone, leading to the rapid formation of mesityl oxide with unexpectedly high reactivity in DMSO.[34] This solvent-mediated acetone activation represents an unusual mode of amino-acid-driven organocatalysis:[33–35] it proceeds under ambient, catalyst-free conditions in non-aqueous media, generates nanoscale-forming hydrophobic products, and reveals a previously unrecognized reactivity landscape fundamentally distinct from classical Maillard chemistry.

Building upon this concept, we previously demonstrated that solvent-mediated, organocatalytic browning of L-tryptophan proceeds through decarboxylation, deamination, and redox reactions, generating intermediates such as tryptamine, indole-3-aldehyde (I3Ald), and I3AA.[34] Notably, this degradative cascade somewhat parallels natural indole biotransformation processes observed in living systems. However, whether individual indole metabolites, or their combinations, can independently drive such browning reactions and form soft nanostructures has not been investigated.

In contrast to our previous studies on amino acid- and protein-based browning systems,[32–36] the present work demonstrates that discrete biogenic indoles can cooperatively reconstitute tryptophan-like organocatalytic behavior through intermolecular acid–base pairing, thereby enabling browning-driven nanoparticle formation without requiring an intrinsic amino-acid framework. We show that tryptamine undergoes spontaneous and progressive browning in DMSO/acetone, whereas I3AA alone remains inert under identical conditions, remarkably, introducing I3AA into the tryptamine system results in strong synergistic acceleration of browning. The resulting browned mixtures spontaneously yield colloidally stable particles upon nanoprecipitation, exhibiting zwitterionic and pH-responsive surface behavior together with electrostatic interaction with nucleic acids. Collectively, these findings introduce a modular organocatalytic strategy for transforming biogenic indoles into functional nanomaterials through solvent-driven browning chemistry.

2. Results and discussion

2.1 Browning reactivity of biogenic indoles and synergistic effect of indole-3-acetic acid

We first evaluated the browning propensity of L-tryptophan (L-Trp), tryptamine (the decarboxylated metabolite of L-Trp), and other structurally related indole derivatives (Fig. 1A) in a DMSO/acetone (9 : 1, v/v) system at room temperature. Among all tested compounds, only tryptamine exhibited a gradual and visually appreciable browning response when reacted alone (Fig. 1B). Notably, when tryptamine was combined with indole-3-acetic acid (I3AA), the reaction proceeded much more rapidly and intensely, producing a dark brown to nearly black solution within just 2 days, indicating strong synergistic enhancement of browning (Fig. 1B).

To quantitatively assess the extent of browning, mesityl oxide (MO), the characteristic self-aldol condensation product of acetone and a validated marker of this browning reaction,[33–35] was monitored by HPLC after 6 days of reaction. MO formation was detected in both L-Trp and tryptamine systems; however, the presence of I3AA markedly amplified its production (Fig. 1C and D), confirming that I3AA accelerates the solvent-mediated browning process.

The observation that tryptamine alone undergoes significant browning in DMSO/acetone is mechanistically unexpected, as it indicates that the coexistence of amine and carboxylate groups within a single molecule, previously considered essential in L-Trp-mediated browning, is not a prerequisite for this chemistry. The further enhancement of browning upon addition of an indole carboxylic acid highlights a critical modulatory role of acid–base pairing among biogenic indoles, suggesting that intermolecular organocatalysis drives acetone condensation and downstream reaction pathways. These results support an expanded view of solvent-mediated browning, wherein mixed indoles cooperatively promote the formation of complex reaction products. Building on this reactivity, we next investigated the consequences of browning degree and indole composition on nanoprecipitation behavior,[33–35] aiming to establish controllable routes for producing colloidally stable nanostructures from biogenic indoles.

2.2 Browning-induced supersaturation as a route to indole nanoparticle formation

Scheme S1 outlines the workflow used to establish controllable nanoparticle formation from browned indole systems. First, the extent of solvent-mediated browning was tuned by varying the concentration of I3AA in tryptamine-containing DMSO/acetone (9 : 1 v/v) mixtures, thereby modulating the accumulation of hydrophobic reaction intermediates in the organic phase. Second, nanoprecipitation was performed by rapidly introducing the browned organic phase into deionized water to trigger supersaturation-driven assembly. Third, the resulting dispersions were subjected to systematic physicochemical characterization (*e.g.*, particle size, zeta potential, and colloidal stability) as a function of reaction composition and browning duration. Notably, this solvent-mediated browning system enables supersaturation-based nanoparticle formation in a single step at room temperature, without the need for additional additives (*e.g.*, polyanions)[37–39] or harsh conditions (*e.g.*, elevated temperature/pH)[40,41] that are often required to generate nanoparticles from Maillard reaction products in conventional aqueous, thermally driven systems.

Fig. S1 shows the progressive browning over time, which was evident for tryptamine-containing reactions but not for I3AA alone. Increasing the I3AA concentration in the organic phase resulted in visibly intensified browning, consistent with enhanced reaction progress. This visual trend was supported by UV-visible spectrophotometric measurements (Fig. S2), where both the rate and magnitude of absorbance growth increased

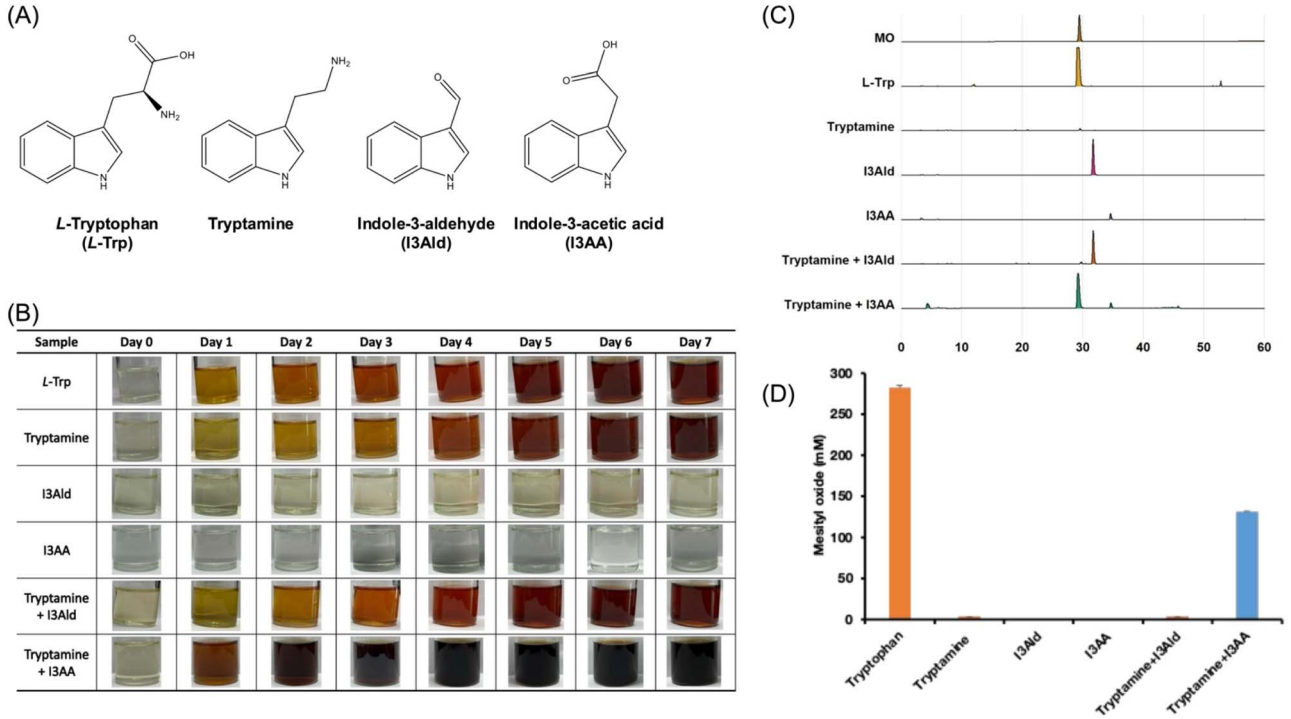

Fig. 1 Comparative analysis of browning reactivity among biogenic indoles. (A) Chemical structures of L-tryptophan (L-Trp), tryptamine, indole-3-aldehyde (I3Ald), and indole-3-acetic acid (I3AA). (B) Time-dependent visual changes of DMSO/acetone (9 : 1, v/v) solutions containing individual or mixed indoles during browning at room temperature (days 0–7). (C) Representative HPLC chromatograms (recorded at 242 nm) showing mesityl oxide (MO) formation as the diagnostic self-condensation product of acetone in the browning system; chromatograms of authentic MO and reaction mixtures (day 6) are shown for comparison. (D) Quantitative comparison of MO formation across different indole systems after 6 days of reaction, highlighting the catalytic enhancement observed in the tryptamine + I3AA combination.

with I3AA content and reaction time. The spectra exhibited a characteristic absorption maximum near 350 nm along with a broad tail into the visible region, indicative of the formation of increasingly conjugated and chromophoric products associated with browning progression.

2.3 Influence of browning extent and I3AA content on colloidal nanoparticle formation

The impact of browning progression and indole composition on colloidal assembly was systematically evaluated by characterizing the hydrodynamic diameters and zeta potentials of particle dispersions formed after nanoprecipitation (Fig. 2). Four organic-phase formulations were examined: tryptamine alone and tryptamine combined with 1, 5 or 10 mg mL^{-1} of I3AA, each subjected to 1–6 days of browning in DMSO/acetone (9; 1, v/v).

For the tryptamine-only system (Fig. 2A), 1 day of browning produced dispersions with broad particle-size distributions and nearly neutral surface charge, consistent with insufficient stabilization and poor colloidal integrity (see also Fig. S3). Browning for ≥2 days enabled successful colloidal particle formation, with particle sizes gradually decreasing and zeta potentials becoming increasingly positive (up to ~+12 mV), indicative of growing surface charge density as the browning reaction proceeded.

Upon incorporation of I3AA (1–10 mg mL^{-1}; Fig. 2B–D & S3), colloidal particles were readily generated even from 1 day browned organic phases. These dispersions exhibited substantially higher positive surface charge (typically ~+20 mV), reflecting the enhanced formation of protonatable groups during the accelerated browning process. Analysis of the corresponding DLS intensity distributions (Fig. S3) showed that most I3AA-containing samples were dominated by a single, primary size population, with no pronounced secondary peaks. At longer browning times, weak and poorly resolved shoulders at larger diameters became occasionally discernible, indicating the onset of minor large-particle fractions, although these features remained marginal and did not develop into clearly separated multimodal distributions.

Across all I3AA-containing systems, prolonged browning yielded progressively smaller mean particle sizes, accompanied by a modest increase in polydispersity index. This trend is consistent with a trade-off between enhanced nucleation, driven by higher concentrations of hydrophobic browning products at greater degrees of reaction, and subsequent growth and coalescence processes that broaden the overall size distribution.[42–45] Thus, while stronger browning promotes more efficient particle formation and surface charge development, it also introduces increased size heterogeneity, motivating further evaluation of colloidal stability to identify optimized formulations.

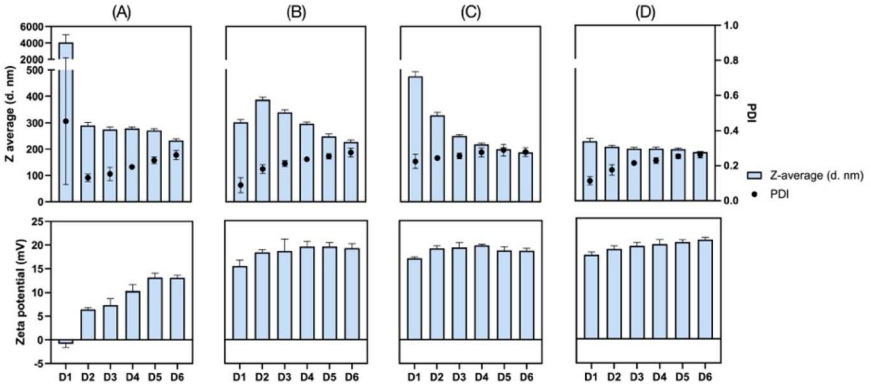

Fig. 2 Systematic evaluation of nanoparticle formation from browned biogenic indole systems. Hydrodynamic diameter and polydispersity index (PDI) (upper panel) and zeta potential (lower panel) of particle dispersions prepared by nanoprecipitation after different browning durations (D1–D6) in DMSO/acetone (9 : 1, v/v). The organic phases contained (A) 10 mg mL^{-1} tryptamine alone, or tryptamine (10 mg mL^{-1}) combined with (B) 1 mg mL^{-1}, (C) 5 mg mL^{-1}, or (D) 10 mg mL^{-1} I3AA. Data are presented as mean ± S.D. of three independent experiments.

2.4 Colloidal stability of indole-derived nanoparticles under storage and thermal stress

The combined effects of higher I3AA content and longer browning duration were shown to promote the formation of smaller and more uniformly charged particles (section 2.3). Since a 4 day browning period yielded an optimal balance between reduced particle size, low polydispersity (Fig. 2), and practical preparation throughput, we adopted this condition for subsequent studies and systematically compared the stability of the resulting colloidal dispersions across all formulation groups under room-temperature storage and accelerated thermal stress.

As shown in Fig. 3A, particles generated from tryptamine alone exhibited limited stability, with rapid particle growth (>1000 nm) occurring within 48 h under ambient conditions. When 1 mg mL^{-1} I3AA group was included (Fig. 3B), the dispersion remained stable during room-temperature storage but failed shortly after exposure to elevated temperature, indicating only marginal improvement in colloidal robustness. In contrast, systems containing 5 or 10 mg mL^{-1} I3AA (Fig. 3C and D) retained both size and surface charge under storage and thermal stress, demonstrating markedly enhanced stability.

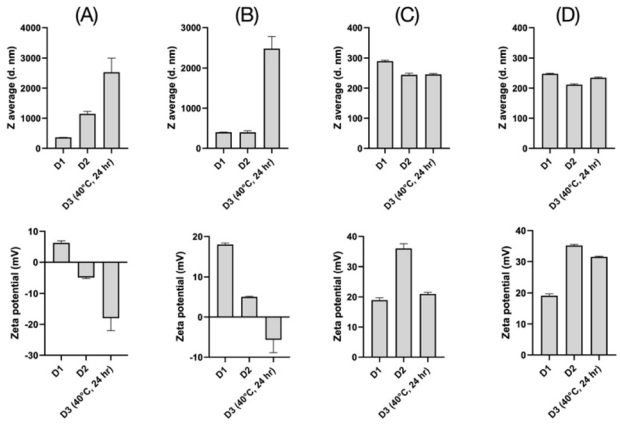

Fig. 3 Colloidal stability testing identifies stable formulations. Particle dispersions were prepared from organic phases containing (A) 10 mg mL^{-1} tryptamine alone, or tryptamine (10 mg mL^{-1}) combined with (B) 1 mg mL^{-1}, (C) 5 mg mL^{-1}, or (D) 10 mg mL^{-1} I3AA. Hydrodynamic diameter (upper panel) and zeta potential (lower panel) were reported as mean ± S.D. of 3 independent experiments measured over two consecutive days (stored at room temperature), followed by an additional 24 h incubation at 40 °C to assess thermal stability and potential aggregation.

Notably, the zeta potentials of the low- and high-I3AA formulations were of comparable magnitude prior to thermal challenge, suggesting that differences in electrostatic stabilization alone cannot fully account for the divergent stability profiles. Instead, we attribute the failure of the low-I3AA systems to a less extensively browned and structurally matured matrix, in which residual reactive or mobile functional groups may remain accessible. Under elevated temperature, such partially condensed networks may undergo thermally accelerated structural rearrangement, interparticle cross-linking, or matrix densification, promoting aggregation despite sufficient nominal surface charge. By contrast, higher I3AA loading likely drives more complete condensation and chemical "locking" of the browned framework, yielding a more rigid, less reactive particle architecture that resists thermal aging.

From a practical perspective, this behavior suggests that the higher-I3AA formulations may be better suited for conditions relevant to biological and formulation environments, where elevated temperature and the presence of electrolytes or biomolecules can further perturb colloidal stability. While these factors were not explicitly modeled here, the enhanced thermal resilience observed at 40 °C provides an initial indication of greater robustness under physiologically relevant stress conditions.

2.5 Physicochemical properties and morphology of optimized formulations

Based on the stability evaluation (section 2.4), two formulations, designated F1 and F2, were selected for detailed characterization as representative systems prepared under the

optimized 4 day browning condition. These formulations were generated using tryptamine (10 mg mL^{-1}) combined with either 5 mg mL^{-1} (F1) or 10 mg mL^{-1} I3AA (F2) in DMSO/acetone (9 : 1, v/v), followed by nanoprecipitation and purification by dialysis. Key physicochemical parameters are summarized in Table S1.

Both formulations exhibited near-neutral dispersion pH (~6.8), high positive zeta potential (~+45 mV), consistent with amine-rich surface chemistry, and low polydispersity indices (PDI ≈ 0.15), indicating well-defined and narrowly distributed particle populations.

F2 displayed a slightly smaller hydrodynamic diameter than F1, consistent with the more extensive browning observed at higher I3AA concentration. From a nucleation perspective, increased production of hydrophobic browning intermediates at higher I3AA loading likely enhances supersaturation during nanoprecipitation, promoting more rapid nucleation and yielding a larger number of smaller particles.[42–45] These differences define a practical formulation window in which particle size, surface charge, and dispersity can be tuned, motivating subsequent evaluation of biological response and functional performance in later sections.

Scanning electron microscopy (Fig. 4) confirmed the formation of predominantly spherical nanoparticles with smooth surface texture. The solid-state diameters observed by SEM were consistent with the hydrodynamic sizes measured by DLS, indicating that the particles maintain their morphology upon drying. The absence of pronounced surface roughness or anisotropic features suggests a reduced propensity for mechanical interlocking between particles, which is consistent with the good colloidal stability observed in dispersion. The observed size variability is in line with a solvent-exchange nanoprecipitation process, which typically yields moderately dispersed particle populations rather than strictly monodisperse systems.

2.6 pH-dependent surface charge regulation and colloidal stability

To further evaluate interfacial properties relevant to colloidal performance in aqueous media, the zeta potential and hydrodynamic diameter of the browned indole-derived nanoparticles were measured across a broad pH range (2–12). As shown in Fig. 5, the nanoparticles underwent a clear charge reversal, transitioning from strongly positive values at acidic pH to negative values under alkaline conditions. The isoelectric point was identified near pH ~9, where charge neutralization coincided with significant increases in particle size, indicative of aggregation near the point of zero charge. Many zwitterionic or charge-reversal nanoparticle systems exhibit isoelectric points closer to physiological pH (~7.4),[46–49] whereas the higher isoelectric point observed here indicates a different distribution and balance of surface-associated functional groups, reflecting the specific chemical composition and heterogeneity of the browned indole matrix.

At pH ≤ 7, the particles maintained high positive zeta potentials (>+30 mV), resulting in robust electrostatic stabilization and stable colloidal dispersion. Upon further alkalinization beyond the isoelectric region, zeta potentials recovered to negative values approaching −40 mV; however, particle aggregation was still observed under strongly basic conditions (pH 11–12). These results suggest that electrostatic repulsion alone is insufficient to counteract destabilizing factors present at elevated pH, potentially including deprotonation-induced changes in the molecular organization of the browned polymeric matrix or base-assisted interparticle interactions.

Overall, the nanoparticles exhibited zwitterionic behavior, consistent with the presence of coexisting amine- and carboxylate-associated functionalities as identified by FTIR (section 2.8).

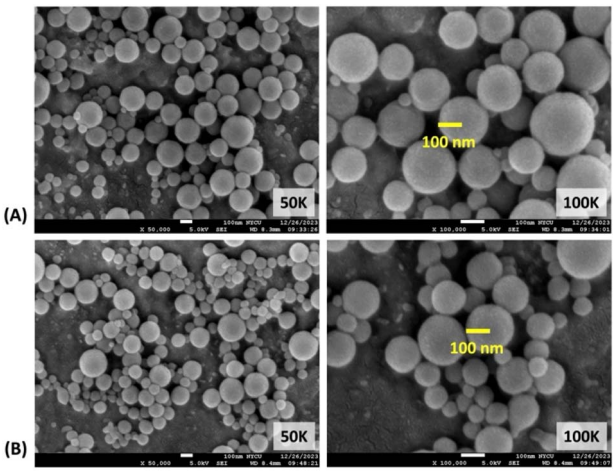

Fig. 4 Representative SEM images of browned indole-derived nanoparticles prepared from (A) F1 and (B) F2 formulations. Images were taken at magnifications of 500 00× (left) and 1 000 00× (right). Scale bars: 100 nm.

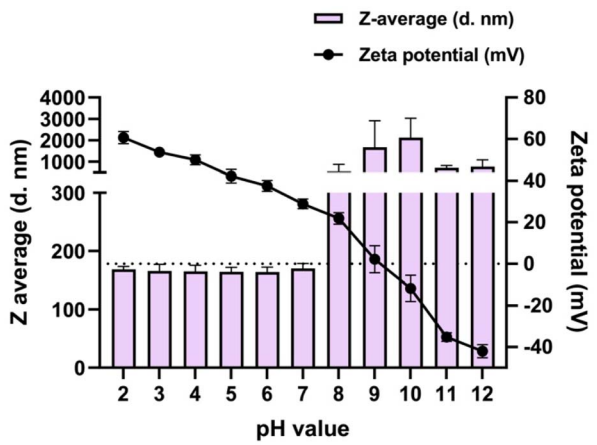

Fig. 5 pH titration reveals zwitterionic surface charge and corresponding colloidal stability. Particle dispersions were prepared from organic phases containing tryptamine (10 mg mL^{-1}) and I3AA (10 mg mL^{-1}). Hydrodynamic diameter and zeta potential were reported as mean ± S.D. of 3 independent experiments measured immediately after pH adjustment using 0.01 N HCl or 0.01 N NaOH.

2.7 Biointerface functionality: cytocompatibility and electrostatic interaction with polynucleotides

The cytocompatibility of the browned indole-derived nanoparticles was evaluated in two cells lines, MDA-MB-231 (human breast carcinoma) and RAW 264.7 (murine macrophage). Fig. S4 presents the viability profiles of both formulations (F1: 10 mg mL^{-1} tryptamine + 5 mg mL^{-1} I3AA; F2: 10 mg mL^{-1} tryptamine + 10 mg mL^{-1} I3AA) across a broad concentration range after 24, 48, and 72 h exposure. At concentrations of approximately 0.005 mg mL^{-1} and below, no appreciable cytotoxicity was observed for either formulation at all incubation times. Cell viability decreased progressively at higher concentrations and with prolonged incubation. Apparently, the browned indole-derived nanoparticles exhibit somewhat higher cytotoxicity than our previously reported amino-acid browning nanoparticle platform (lysine–cysteine system),[33] although direct comparison is limited by differences in the cell models and experimental conditions.

Fig. S5 shows that formulation F2 was slightly less cytotoxic than F1 in both cell models (IC_{50}: F1 = 0.008 *vs.* F2: 0.010 mg mL^{-1} for RAW 264.7; F1 = 0.007 *vs.* F2 = 0.011 mg mL^{-1} for MDA-MB-231) and was therefore selected for further functional evaluation.

To explore their capability to engage in biomolecular interactions, the nanoparticles were incubated with G3139, an 18-mer phosphorothioate antisense oligonucleotide.[50] As summarized in Fig. 6, electrostatic association between the cationic nanoparticle surface and the anionic nucleic acid resulted in measurable entrapment efficiencies, which increased with nanoparticle concentration, incubation time, and acidic pH conditions where positive surface charge is maximized. Notably, complex formation led to reversal of zeta potential from positive to negative, reflecting polyelectrolyte adsorption at the particle interface. Importantly, the hydrodynamic dimensions of the nanoparticle–G3139 complexes remained essentially unchanged (Fig. S6), indicating stable nanoscale assembly without significant aggregation. Under the optimized conditions examined here, the maximum entrapment efficiency reached approximately 50%, which is lower than the ~90% efficiency previously reported for our lysine–cysteine browning nanoparticle platform,[33] although direct quantitative comparison is limited by differences in formulation composition and experimental conditions. The ability to form stable complexes with polyanionic cargo nevertheless highlights the functional versatility of this indole-derived nanoparticle system for applications requiring controlled colloidal interactions in aqueous environments.

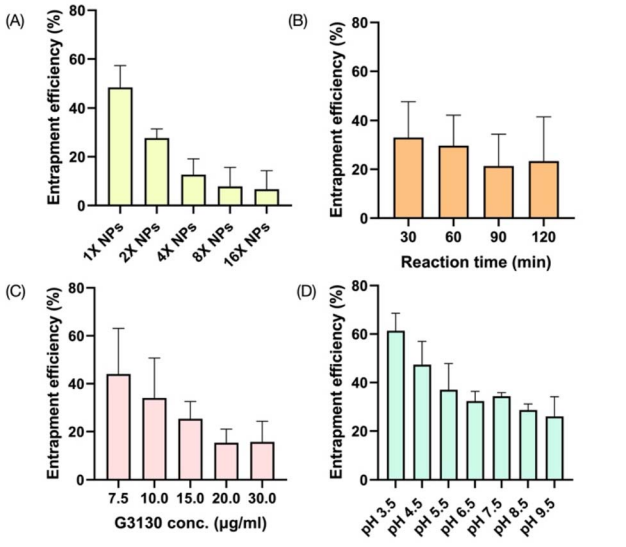

Fig. 6 Modulation of nanoparticle–polynucleotide interactions under varying conditions. Entrapment efficiency of G3139 (mean ± SD, $n = 3$) as a function of (A) nanoparticle concentration (dilution factors 1*X*–16*X*), (B) incubation time, (C) G3139 concentration, and (D) solution pH. Nanoparticles were prepared from browned organic phases containing tryptamine (10 mg mL^{-1}) and I3AA (10 mg mL^{-1})

2.8 Spectroscopic and reaction-pathway insights into solvent-mediated indole browning

FTIR analysis provided molecular-level evidence of the compositional changes associated with indole browning and nanoparticle formation (Fig. S7). Key vibrational signatures from both tryptamine and I3AA remained detectable in the nanoparticle spectrum, including indole N–H stretching (~3400 cm^{-1}), amine stretching modes (3300–3200 cm^{-1}), C–N stretching (~1300 cm^{-1}), and C–H out-of-plane bending (~740 cm^{-1}). Carbonyl contributions from I3AA were also observed near 1710–1720 cm^{-1}.[51,52] In contrast to the precursor molecules, the nanoparticle spectrum displayed a broad absorption envelope spanning ~1700–1000 cm^{-1}, reflecting extensive band overlap and loss of peak resolution, consistent with the formation of chemically heterogeneous and cross-linked browning products. The coexistence of amine- and carboxylate-associated bands is consistent with the amphoteric surface chemistry inferred from zeta-potential measurements, whereby both functionalities contribute to the observed pH-dependent charge reversal, isoelectric behavior, and the capacity to form polyelectrolyte complexes with polyanionic species such as G3139. However, the detailed chemical structures and spatial distribution of these functional groups within the browned matrix remain to be fully resolved.

HPLC monitoring further elucidated the reaction mechanism (Fig. 7). In the mixed-indole system, mesityl oxide (MO)—a marker of acetone self-condensation—emerged immediately and accumulated continuously over 96 h, whereas MO formation in the tryptamine-only system exhibited a delayed onset (>24 h; Fig. S8 and S9). Meanwhile, I3AA concentration remained largely unchanged, indicating that it functions catalytically rather than as a consumed substrate. Concurrent evolution of strongly retained chromatographic peaks supports the formation of hydrophobic browning products capable of spontaneous nanoparticle assembly during nanoprecipitation.

Together, these findings support a cooperative organocatalytic mechanism in which I3AA serves as an acidic promoter while tryptamine provides complementary basic functionality. This intermolecular acid–base pairing reconstitutes the

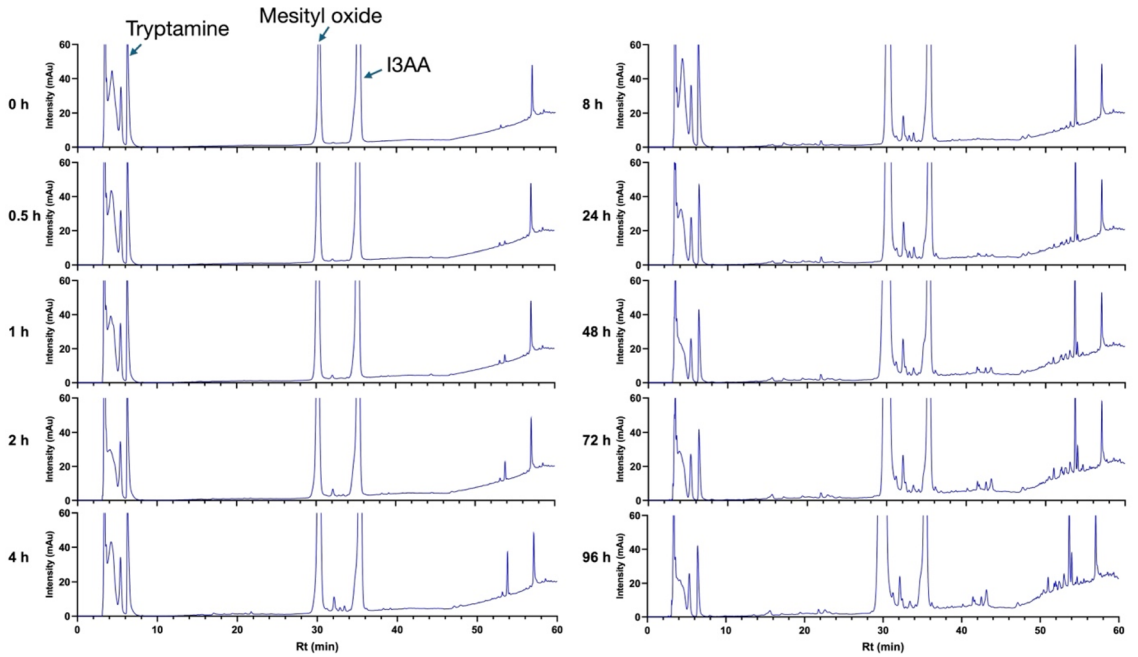

Fig. 7 Time-evolved HPLC chromatograms of the browning reaction in mixed indole systems. Chromatographic profiles of the organic phase containing tryptamine (10 mg mL^{-1}) and I3AA (10 mg mL^{-1}) during solvent-mediated browning in DMSO/acetone (9 : 1, v/v) over 0–96 h. The major product, mesityl oxide (MO), and the starting materials were identified using authentic standards. Over time, tryptamine peaks progressively decreased, whereas I3AA peaks remained nearly constant. In contrast, the MO peak appeared immediately and grew continuously.

catalytic behavior previously observed for L-tryptophan,[34] thereby accelerating browning and enabling rapid generation of hydrophobic species that supersaturate and nucleate into nanoparticles. Such a solvent-driven transformation highlights a modular chemical strategy by which simple biogenic indoles reorganize into emergent colloidal soft-matter structures.

3. Conclusions

This study demonstrates a solvent-mediated organocatalytic strategy for transforming biogenic indoles into colloidal soft-matter assemblies. In contrast to our earlier amino acid- and protein-based browning systems,[32–36] we show that tryptamine undergoes spontaneous browning in a DMSO/acetone medium, while indole-3-acetic acid (I3AA) acts cooperatively to accelerate acetone self-condensation and the formation of hydrophobic browning products that yield nanoparticles upon nanoprecipitation. The key conceptual advance lies in reconstructing tryptophan-like catalytic behavior through intermolecular pairing of two discrete indole derivatives, demonstrating that an intrinsic amino-acid framework is not required for solvent-mediated browning or the subsequent formation of colloidal particles. The resulting browned indole-derived particles exhibit tunable size, positive surface charge, pH-responsive behavior, and the ability to associate electrostatically with polyanionic biomolecules, highlighting the potential of modular biogenic indole combinations as a versatile platform for generating functional colloidal materials.

Several limitations of the present study should be noted. First, the detailed chemical structures of browned products remain incompletely resolved, and further structural elucidation using complementary techniques such as LC-MS/HRMS and NMR would help refine mechanistic understanding of the browning process. Second, the biological evaluation presented here is limited to *in vitro* cytotoxicity and interaction with a single oligonucleotide model. Finally, the behavior of these nanoparticles in complex physiological environments (*e.g.*, high ionic strength or serum-containing media) also remains to be examined. Addressing these aspects will be important for further development and application of this emerging browning-derived nanoparticle platform.

4. Experimental

4.1 Materials

Tryptamine (≥97%), indole-3-acetic acid (I3AA; 98%), and indole-3-aldehyde (I3Ald; 97%) were purchased from Sigma-Aldrich (USA). Acetone (99.8%) was obtained from Honeywell (USA), and dimethyl sulfoxide (DMSO; ≥99.9%) from J. T. Baker (USA). Mesityl oxide (99%) was supplied by ACROS Organics (Belgium). Cell culture media and related reagents were purchased from Corning (USA). The antisense oligonucleotide G3139 (sequence: 5′-TCT CCC AGC GTG CGC CAT-3′; phosphorothioate backbone; thiol-modified) was synthesized by Alpha DNA (Canada). Unless otherwise specified, all other chemicals, solvents, and salts were of analytical or HPLC grade and obtained from Sigma-Aldrich or J.T. Baker. Deionized water (resistivity ≥18.2 MΩ cm; ELGA PURELAB, UK) was used for all experiments.

4.2 Browning reaction of biogenic indoles

Browning reactions of biogenic indoles were performed following a general protocol previously optimized for amino acids and proteins.[32] Briefly, indole derivatives were dissolved in a solvent mixture of dimethyl sulfoxide (DMSO) and acetone at a volume ration of 9 : 1 (v/v). The resulting solutions were allowed to stand without mechanical agitation under ambient laboratory conditions (23–24 °C) to initiate solvent-mediated browning. Unless otherwise specified, the reaction time for preparing the browning organic phase was 4 days, which was used as the standard condition for subsequent nanoparticle formation by simple nanoprecipitation.

4.3 Comparative browning reactivity of biogenic indoles

The browning propensity of tryptamine, indole-3-acetic acid (I3AA), and indole-3-aldehyde (I3Ald) was compared with that of L-tryptophan at a fixed concentration of 10 mg mL^{-1} in the DMSO/acetone (9; 1, v/v) mixture. In addition, the combination systems containing tryptamine with I3AA or tryptamine with I3Ald were evaluated under identical conditions. The progression of browning was monitored visually and spectroscopically on a daily basis for up to 7 days.

To further assess relative reactivity, the formation of mesityl oxide (MO), self-aldol condensation product of acetone and a signature marker of this solvent-mediated reaction, was quantified using a previously established HPLC method.[34]

4.4 Synergistic browning of tryptamine with I3AA and nanoparticle preparation

The synergistic browning of tryptamine with indole-3-acetic acid (I3AA) and the corresponding conditions for nanoparticle synthesis were evaluated and optimized following the procedure summarized in Scheme S1. Briefly, tryptamine (10 mg mL^{-1}) and I3AA (1, 5, or 10 mg mL^{-1}) were dissolved in 2 mL of a DMSO/acetone (9 : 1, v/v) mixture and allowed to react for 1–6 days under ambient laboratory conditions. At the designated reaction time, the browned organic phase was added dropwise into 10 mL of deionized water (stirred at 300 rpm) within 15 s, followed by an additional 15 s of stirring. The mixture was then allowed to age without stirring at room temperature for 1 h. The resulting particle dispersions were purified by dialysis against deionized water using a 12–14 kDa molecular-weight-cut-off (MWCO) membrane (Spectral/Por®, Thomas Scientific, USA) at 300 rpm for 24 h.

Throughout the optimization process, both the extent of organic-phase browning and the properties of the resulting nanoparticles were continuously monitored. Browning intensity was assessed visually and spectrophotometrically (Spark 10 M, Tecan, Austria). For the particle dispersions obtained before and after purification, *z*-average hydrodynamic diameter and zeta potential were determined by dynamic light scattering (Zetasizer Nano ZS90, Malvern, UK).

Finally, the optimal formulation was further identified based on colloidal stability testing, in which particle size and zeta potential were monitored under both room-temperature and accelerated stress conditions (40 °C).

4.5 Characterization of optimized nanoparticle formulations

The optimized nanoparticle formulations were characterized for their physicochemical properties, including pH, hydrodynamic diameter, polydispersity index (PDI), and zeta potential. Particle morphology was examined by scanning electron microscopy (SEM; JSM-7600F, JEOL, Japan) using samples air-dried on copper specimen stubs prior to imaging.

4.6 Surface charge properties and pH-dependent colloidal stability

Browned indole-derived nanoparticle dispersions were prepared using tryptamine and I3AA (each at 10 mg mL^{-1}) following the general preparation procedure. The dialysis-purified dispersions were subjected to pH titration over the pH 2–12 using 0.0 N HCl or 0.01 N NaOH solutions. The resulting dispersions were examined for aggregation or sedimentation behavior, and their hydrodynamic diameter, polydispersity index (PDI), and zeta potential were measured to establish the pH-dependent colloidal stability profile.

4.7 Evaluation of cytotoxicity

4.7.1 Cell culture conditions. MDA-MB-231 (human breast carcinoma; BCRC 60425) and RAW 264.7 (murine macrophage; BCRC 60001) cells were obtained from the BCRC (Taiwan) and cultured in Dulbecco's Modified Eagle Medium (DMEM) containing 10% (v/v) fetal bovine serum (FBS) and 1% penicillin–streptomycin. Cultures were kept in tissue culture dishes at 37 °C in a humidified incubator with 5% CO_2. Upon reaching approximately 90% confluence, the culture medium was removed and cells were rinsed twice with 12 mL phosphate-buffered saline (PBS). Cells were detached using 2 mL of 0.05% trypsin, incubated for 5 min, and then neutralized with 2 mL DMEM. The resulting cell suspension was diluted with 6 mL PBS and centrifuged at 1000 rpm for 5 min to remove the supernatant. The resulting cell pellet was resuspended in fresh DMEM for subsequent experiments.

4.7.2 Nanoparticle treatment and MTT assay. Cells were seeded in 96-well plates at a density of 2×10^4 cells per well (200 μL) and allowed to adhere for 24 h. The culture medium was then replaced with 200 μL of nanoparticle dispersions prepared in DMEM at various concentrations (w/v). The dry weight of nanoparticles in the stock dispersions was determined by the weight loss on drying method, in which samples were dried to constant weight (defined as ≤0.05% difference between two consecutive measurements).

The nanoparticle dispersions were serially diluted at factors of 10, 18, 32, 56, 100, 180, 320, 560, and 1000, chosen to achieve approximately equal spacing on a logarithmic concentration scale. Treated cells were incubated for 24, 48, or 72 h, followed by removal of the nanoparticle dispersions. Cells were then incubated with 100 μL of MTT solution (0.5 mg mL^{-1}) for 3 h. After incubation, the MTT solution was removed, and 100 μL of

DMSO was added to each well to dissolve the resulting formazan crystals. The absorbance was measured at 570 nm using a microplate reader (Tecan Spark 10 M, Austria). Cell viability (%) was calculated as the percentage of absorbance of the treated cells relative to that of the untreated control cells.

4.8 Nanoparticle–polynucleotide interaction

The antisense oligonucleotide G3139 (sequence: 5′-TCT CCC AGC GTG CGC CAT-3′), an 18-mer phosphorothioate oligodeoxynucleotide, was used as a model polynucleotide. The nanoparticle formulation employed was prepared from tryptamine and I3AA (each at 10 mg mL^{-1}). Unless otherwise specified, nanoparticle dispersions were mixed with G3139 solutions and incubated for 30 min at room temperature. The mixtures were then centrifuged at 30 000×*g* for 30 min, and the supernatants were collected for quantifying the concentration of unbound (free) G3139. Quantification was performed spectrophotometrically at 260 nm using a NanoDrop spectrophotometer (ND-1000, Thermo Fisher Scientific, USA), based on a calibration curve of G3139.

To evaluate the factors influencing binding, four parameters were systematically varied: nanoparticle concentration, G3139 concentration, incubation time, and pH. The entrapment efficiency (EE%) was calculated as:

$$EE\% = 100 \times ([G3139]_{added} - [G3139]_{free})/[G3139]_{added}$$

The resulting nanoparticle–G3139 complexes were further characterized by dynamic light scattering (DLS) to determine changes in hydrodynamic diameter and zeta potential, providing insight into electrostatic complexation behavior.

4.9 FTIR analysis of chemical functionality

Fourier-transform infrared (FTIR) spectroscopy was employed to identify the chemical functionalities present in the browned indole-derived nanoparticles. Lyophilized nanoparticle powders were analyzed using a Shimadzu IR-Affinity-1S FTIR spectrophotometer equipped with an ATR (ZnSe) accessory. Spectra were recorded in the 4000–650 cm^{-1} range at a resolution of 2 cm^{-1}. The spectral features of the nanoparticles were compared with those of the starting materials, *i.e.*, tryptamine and indole-3-acetic acid (I3AA), to identify characteristic functional groups and assess chemical transformations associated with browning.

4.10 HPLC profiling of browning reactivity

The kinetics and product evolution of the browning reaction in DMSO/acetone (9 : 1, v/v) were examined and compared for tryptamine alone (10 mg mL^{-1}) and the tryptamine–I3AA combination (each 10 mg mL^{-1}) using a previously established HPLC method.[34] The reaction was initiated by dissolving the biogenic indoles in the solvent mixture at room temperature, followed by sampling 1 mL aliquots at 0, 0.5, 1, 2, 4, 8, 24, 48, 72, and 96 h. Each aliquot was immediately quenched by adding 100 μL of deionized water[32] and stored at −80 °C until analysis.

Prior to injection, samples were diluted 25-fold with methanol and analyzed on an Agilent 1260 Infinity II HPLC system equipped with a diode array detector (DAD) and a Mightysil ODS column (4.6 mm × 250 mm, 5 μm), with the column temperature maintained at 25 °C, under a gradient reverse-phase elution program. Chromatograms were recorded at 242 nm, corresponding to the maximum absorbance of mesityl oxide (MO), the diagnostic product of acetone self-condensation. Comparative chromatographic profiles were used to evaluate reaction progress, MO formation, and the evolution of browning-related species.

Author contributions

TMH: conceptualization, methodology, visualization, resources, writing – original draft, review & editing, supervision, project administration, funding Acquisition. HHL: investigation, validation, formal analysis, data curation, visualization. CYH: methodology, investigation, formal analysis, data curation, visualization. MHL: validation, supervision. SJC: resources, supervision.

Conflicts of interest

There are no conflicts to declare.

Data availability

The data supporting this article have been included as part of the supplementary information (SI). Supplementary information is available: Scheme S1, Fig. S1–S9 and Table S1. See DOI: https://doi.org/10.1039/d5ra09863g.

Acknowledgements

This work was supported by the National Science and Technology Council, Taiwan [MOST 111-2320-B-A49-020-MY3]

Notes and references

1 R. Silva Moratório de Moraes, A. B. Mestre Botelho, G. Tavares de Almeida Pinto, S. Couto Rodrigues, M. T. Miranda Martins, D. L. Alves Soares, C. Cardoso Cruz, A. de Almeida Pinto, F. Rodrigues Fintelman Dias, P. Dias Fernandes and A. C. Cunha, *Chem. Rec.*, 2025, **25**, e202500121.
2 A. Kumar, A. B. Dapkekar and G. Satyanarayana, *Org. Biomol. Chem.*, 2025, **23**, 9222–9256.
3 B. A. Babalola, M. Malik, O. Olowokere, A. Adebesin and L. Sharma, *Eur. J. Med. Chem. Rep.*, 2025, **13**, 100252.
4 C. M. Drăgoi, A.-C. Nicolae and I.-B. Dumitrescu, *Targets*, 2026, **4**, 4.
5 H. Maeda and N. Dudareva, *Annu. Rev. Plant Biol.*, 2012, **63**, 73–105.
6 Y. Zhao, *Annu. Rev. Plant Biol.*, 2010, **61**, 49–64.
7 T. Zelante, M. Puccetti, S. Giovagnoli and L. Romani, *Curr. Opin. Immunol.*, 2021, **70**, 27–32.

8 K. Gao, C.-l. Mu, A. Farzi and W.-y. Zhu, *Adv. Nutr.*, 2020, **11**, 709–723.
9 J. Yan, D. Chen, Z. Ye, X. Zhu, X. Li, H. Jiao, M. Duan, C. Zhang, J. Cheng, L. Xu, H. Li and D. Yan, *Mol. Cancer*, 2024, **23**, 241.
10 Y. Lai, C.-W. Liu, L. Chi, H. Ru and K. Lu, *ACS Omega*, 2021, **6**, 8094–8103.
11 Y. Wang, Y. Hua, S. Chen, H. Wang, Y. Li, C. Chen, Y. Zhu, Y. Zhang and X. Dai, *J. Environ. Manage.*, 2026, **397**, 128375.
12 M. Ward and N. M. O'Boyle, *RSC Med. Chem.*, 2025, **16**, 4540–4570.
13 A. Fernando Rodrigues de Sa, J. B. Eliezer and F. Carlos Alberto Manssour, *Mini-Rev. Med. Chem.*, 2009, **9**, 782–793.
14 A. Kumari and R. K. Singh, *Bioorg. Chem.*, 2019, **89**, 103021.
15 E. Barresi, M. Robello, E. Baglini, V. Poggetti, M. Viviano, S. Salerno, F. Da Settimo and S. Taliani, *Pharmaceuticals*, 2023, **16**, 997.
16 E. Vitaku, D. T. Smith and J. T. Njardarson, *J. Med. Chem.*, 2014, **57**, 10257–10274.
17 X. Mo, D. P. Rao, K. Kaur, R. Hassan, A. S. Abdel-Samea, S. M. Farhan, S. Bräse and H. Hashem, *Molecules*, 2024, **29**, 4770.
18 S. K. Burley and G. A. Petsko, *Science*, 1985, **229**, 23–28.
19 K. Madhusudan Makwana and R. Mahalakshmi, *Protein Sci.*, 2015, **24**, 1920–1933.
20 L. Guo, W. Li, Z. Gu, L. Wang, L. Guo, S. Ma, C. Li, J. Sun, B. Han and J. Chang, *Int. J. Mol. Sci.*, 2023, **24**, 4360.
21 I. M. Stanković, S. Niu, M. B. Hall and S. D. Zarić, *Int. J. Biol. Macromol.*, 2020, **156**, 949–959.
22 X. Song, S. He, J. Zheng, S. Yang, Q. Li and Y. Zhang, *Molecules*, 2023, **28**, 3334.
23 X. Song, J. Zheng, S. He, Y. Liu, S. Yang, Q. Li, C. Liu, Z. Zhang, X. Liu, C. Deng and Y. Zhang, *Chin. Chem. Lett.*, 2023, **34**, 108069.
24 A. K. Nguyen, T. G. Molley, E. Kardia, S. Ganda, S. Chakraborty, S. L. Wong, J. Ruan, B. E. Yee, J. Mata, A. Vijayan, N. Kumar, R. D. Tilley, S. A. Waters and K. A. Kilian, *Nat. Commun.*, 2023, **14**, 6604.
25 N. Nakatsuka, M. M. Hasani-Sadrabadi, K. M. Cheung, T. D. Young, G. Bahlakeh, A. Moshaverinia, P. S. Weiss and A. M. Andrews, *ACS Nano*, 2018, **12**, 4761–4774.
26 K. Jeon, N. M. O. Andoy, D. Dufour, J. Y. C. Yang, C. M. Lévesque and R. M. A. Sullan, *ACS Infect. Dis.*, 2024, **10**, 3176–3184.
27 K. Ishino, S. Nishitani, Y. Man, A. Saito and T. Sakata, *Langmuir*, 2022, **38**, 8633–8642.
28 L. El Hosry, V. Elias, V. Chamoun, M. Halawi, P. Cayot, A. Nehme and E. Bou-Maroun, *Foods*, 2025, **14**, 1881.
29 A. Shakoor, C. Zhang, J. Xie and X. Yang, *Food Chem.*, 2022, **393**, 133416.
30 Y. Bao, H. Gou, G. Sánchez-Terrón, L. Zhang, R. Zamora, F. J. Hidalgo and M. Estévez, *Food Chem.*, 2025, 146446.
31 S. Bolchini, L. Angeli, G. Ferrentino, M. Van Boekel, R. Amorati, M. Scampicchio and K. Morozova, *Lwt*, 2025, **217**, 117316.
32 T.-M. Hu and Y.-H. Chiang, *Biochem. Biophys. Res. Commun.*, 2021, **536**, 67–72.
33 T.-M. Hu, J.-A. Liang and Y.-H. Chiang, *J. Mater. Chem. B*, 2024, **12**, 6410–6423.
34 C.-Y. Huang, H.-W. Liao and T.-M. Hu, *RSC Adv.*, 2023, **13**, 29802–29808.
35 T.-M. Hu and W.-Y. Lin, *Colloids Surf., A*, 2025, 139015.
36 C.-J. Chang, M.-C. Li and T.-M. Hu, *Int. J. Biol. Macromol.*, 2026, **344**, 150425.
37 H. Zhang, Y. Zhang, E. Bao and Y. Zhao, *Int. J. Biol. Macromol.*, 2016, **89**, 287–296.
38 S. Viturat, M. Thongngam, N. Lumdubwong, W. Zhou and U. Klinkesorn, *Ultrason. Sonochem.*, 2023, **97**, 106466.
39 C. Jori, A. Ahmad, A. Kumar, B. Kumar, A. Ali, N. Ali, H. Tabassum and R. Khan, *Carbohydr. Polym.*, 2025, **359**, 123537.
40 D. Li, Y. Xie, X. Na, Y. Li, C. Dai, Y. Li and M. Tan, *Food Funct.*, 2019, **10**, 4414–4422.
41 Q. Lin, M. Li, L. Xiong, L. Qiu, X. Bian, C. Sun and Q. Sun, *Food Hydrocolloids*, 2019, **92**, 86–93.
42 X. Yan, J. Bernard and F. Ganachaud, *Adv. Colloid Interface Sci.*, 2021, **294**, 102474.
43 E. Lepeltier, C. Bourgaux and P. Couvreur, *Adv. Drug Delivery Rev.*, 2014, **71**, 86–97.
44 S. M. D'Addio and R. K. Prud'homme, *Adv. Drug Delivery Rev.*, 2011, **63**, 417–426.
45 N. T. K. Thanh, N. Maclean and S. Mahiddine, *Chem. Rev.*, 2014, **114**, 7610–7630.
46 Y. Y. Yuan, C. Q. Mao, X. J. Du, J. Z. Du, F. Wang and J. Wang, *Adv. Mater.*, 2012, **24**, 5476–5480.
47 E. Deiss-Yehiely, G. Cárcamo-Oyarce, A. G. Berger, K. Ribbeck and P. T. Hammond, *ACS Biomater. Sci. Eng.*, 2023, **9**, 4794–4804.
48 S. Hou, Y. Liu, J. Yan, Z. Fang, Y. Gong, Q. Zhang and Y. Yan, *Macromol. Chem. Phys.*, 2025, e00106.
49 W. He, J. Wen, Q. Hu, Y. Yi, Z. Wei, X. Yang, G. Zhai, F. Li and L. Ye, *Int. Mater. Rev.*, 2025, 09506608251323568.
50 S.-J. Chiu, S. Liu, D. Perrotti, G. Marcucci and R. J. Lee, *J. Controlled Release*, 2006, **112**, 199–207.
51 B. B. Ivanova, *Spectrochim. Acta, Part A*, 2006, **64**, 931–938.
52 J. Coates, *Encyclopedia of Analytical Chemistry*, 2000, 12, pp. 10815–10837.